Computational study of a bluff body aerodynamics: impact of the laminar-to-turbulent transition modelling.

F. Rizzo[1*], V. D'Alessandro[2], S. Montelpare[1], L. Giammichele[2]

[1] Department of Engineering and Geology, G. d'Annunzio University of Chieti-Pescara, viale Pindaro 42, 65127, Pescara, Italy
[2] Department of Industrial Engineering and Mathematical Sciences, Università Politecnica delle Marche, via Brecce Bianche, 60131 Ancona, Italy.
* Corresponding author: fabio.rizzo@unich.it

Abstract

The paper discusses the computational fluid dynamics simulation results of a bluff body. A literature case regarding a closed box section of a suspended bridge was selected since it is of practical relevance. An OpenFOAM implementation of a Spalart-Allmaras local correlation based transition model for Reynolds Averaged Navier-Stokes (RANS) equations was used as flow model. Locally-formulated RANS transition models were coupled with the Spalart-Allmaras (SA) model to reduce the computational cost with respect to the SST $k-\omega$ model. This model, named $\gamma - R_{\widetilde{\theta},t}$-SA, was successfully applied on airfoil sections and results are given by literature. In this paper, we present a set of computations of the flow field around a bluff body in order to stress the need to take into account transition effects in these kind of applications. The measure of the proposed model reliability was attested comparing experimental pressure coefficients and aerodynamic forces on the bridge section; besides, the effects of the model predictions on the critical flutter velocity, estimated by FEM and 2DOF Scanlan model of a pedestrian bridge structure, was examined as case of study.

Keywords

Spalart-Allmaras, bridge aerodynamics, fluid mechanics, wind tunnel, CFD.

Graphical abstract

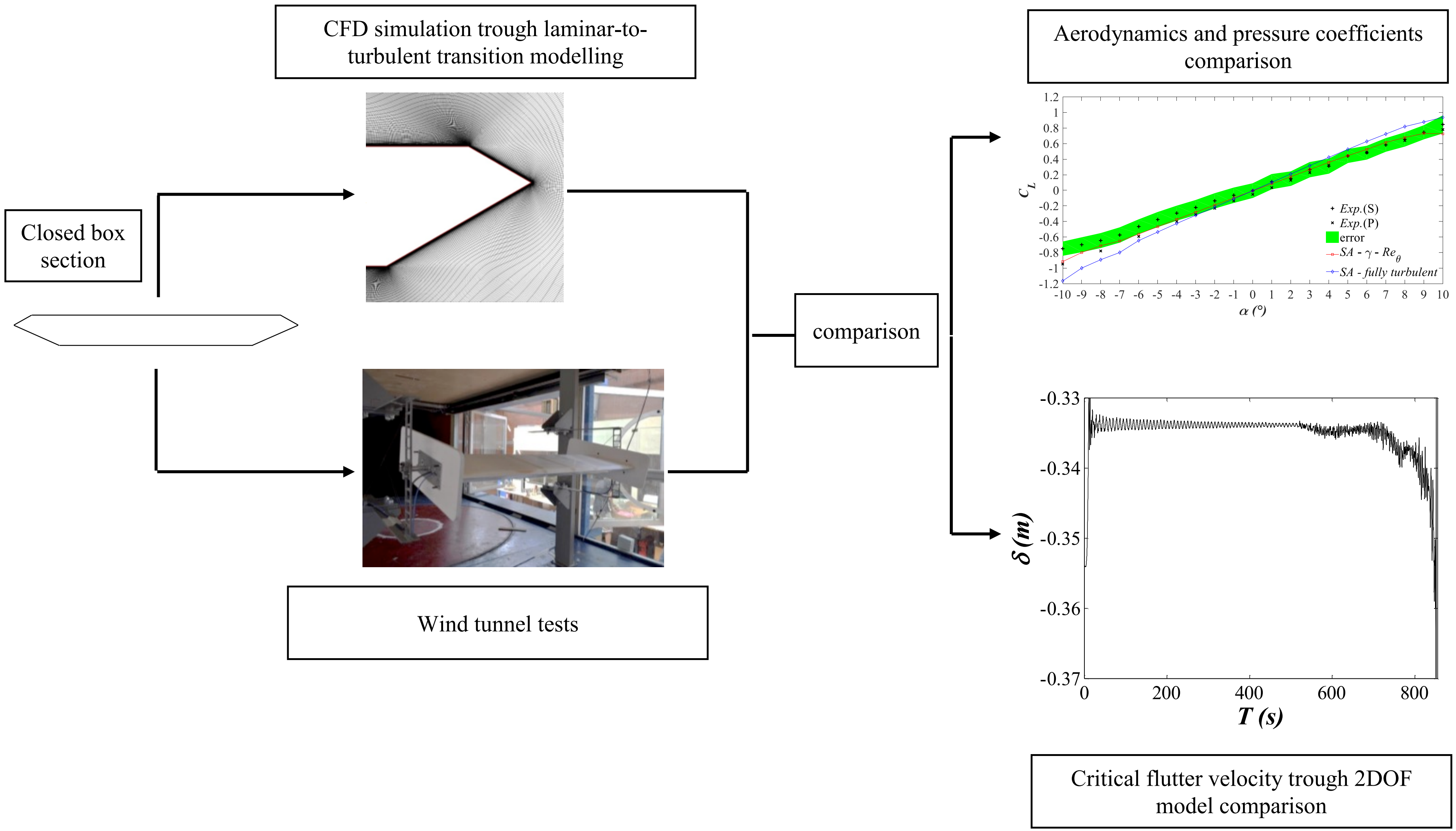

Main symbols

γ	Intermittency
γ_{eff}	Effective intermittency
λ_θ	Thawaites' pressure gradient coefficient
Re	Reynolds number
R_v	Vorticity Reynolds number
$R_{\theta,c}$	Critical Reynolds number
$R_{\theta,t}$	Transition onset momentum thickness Reynolds number
R_T	Viscosity ratio
ν	Molecular viscosity
ν_T	Turbulent viscosity
$\tilde{\nu}$	Modified turbulent viscosity
$\tilde{\nu}_\infty$	Free-stream modified turbulent viscosity
Ω	Vorticity tensor module
S	Strain rate tensor module
ω	Specific dissipation rate
$\tilde{Re}_{\theta_t}$	local transition onset momentum thickness Reynolds number
Tu	Turbulence intensity
Tu_∞	Free-stream turbulence intensity
u_τ	Friction velocity
$\gamma - \tilde{R}_{\theta,t}$	Locally-formulated RANS transition models
$\gamma - \tilde{R}_{\theta,t} - SA$	Locally-formulated RANS transition models coupled with the Spalart-Allmaras (SA)
y^+	Dimensionless first cell height
u_τ	Friction velocity
τ_w	Wall shear stress
u	The velocity vector
p	The pressure divided by the density
f_w	function
d	Wall distance
γ_{sep}	Separation induced intermittency
γ	intermittency function
$F_{reattach}$	function
F_{onset}	function
F_{length}	function
F_{turb}	function

$F_{\theta,t}$	function
$F(\lambda_\theta)$	function
χ	function
f_{v1}	function
f_{v2}	function
g	function
r	function
$\tilde{S}$	function
Ω	Vorticity tensor module
S	Strain rate tensor module
D	Strain rate tensor
W	Vorticity tensor
P_γ	function
T	Constant
D_γ	function
σ_f	Constant
$P_{\theta,t}$	Constant
$\sigma_{\theta,t}$	Constant
c_{w_1}	Constant
c_{w_2}	Constant
c_{w3}	Constant
c_{b_1}	Constant
c_{b_2}	Constant
c_{v_1}	Constant
σ	Constant
k	Constant
c_{a_1}	Constant
c_{e_1}	Constant
c_{a_2}	Constant
c_{e_2}	Constant
$\sigma_{\theta,t}$	Constant
λ_θ	Thwaites' pressure gradient coefficient
C_p	Pressure coefficient
$C_{p,max}$	Maximum of pressure coefficient time history

$C_{p,m}$	Mean of pressure coefficient time history
$C_{p,min}$	Minimum of pressure coefficient time history
$C_{p,\mathrm{k}}$	The pressure coefficient 5% quantile
σ_{C_p}	Standard deviation of pressure coefficient time history
N	Number of non-Gaussian processes
k_{cp}	Excessive kurtosis of pressure coefficient time history
γ_{cp}	Skewness of pressure coefficient time history
p_i	static pressures measured at each pressure tap
p_0	the reference flow static pressure p_0
ρ	Air density
U	Flow speed
D	Drag force
L	Lift force
M	Torsional Moment
B	Deck chord
C_D	Drag coefficient
C_L	Lift coefficient
C_M	Moment coefficient
$\boldsymbol{h_1}$, $\boldsymbol{h_2}$, $\boldsymbol{d_1}$, $\boldsymbol{b_1}$, $\boldsymbol{d_2}$, $\boldsymbol{b_2}$	Deck cross section geometrical dimensions
F_x and F_z	The drag and lift components in agreement with the *x-z* system of reference
G	Deck cross section center of gravity
U_∞	Wind velocity
X	critical reduced frequency ratio
ω	circular frequency of vibration
ω_{v1}	vertical deck mode circular frequency
ω_{t1}	torsional deck mode circular frequency
ω_c	critical circular frequency
ω_a	torsional circular frequency (wind tunnel model)
ω_h	vertical circular frequency (wind tunnel model)
$\delta(x,t)$	vertical oscillation of the simulated bridge deck
$\acute{h}(x,t)$	vertical velocity of the simulated bridge deck
K	reduced frequency
L_1	distance between the tower foundations
L_2	main cable span
L_3	width of the tower foundation legs

f	Bridge main cable sag
$L_h(x,t)$	Aeroelastic lift force per unit length
l	Central span length of the simulated bridge
$M_h(x,t)$	Aeroelastic moment force per unit length
A	deck closed box section area
$A^{\blacksquare}_{1,\ldots,4}$	Flutter derivatives per unit length, torsional moment
$H^{\blacksquare}_{1,\ldots,4}$	flutter derivatives per unit length, lift force
H_1	Distance between the top of the tower and the deck
H_2	Ground level of the deck
t	time variable
U_c	critical velocity
$\alpha(x,t)$	Deck torsional vibration of the simulated bridge
$\acute{\alpha}(x,t)$	Deck torsional velocity of the simulated bridge
ζ	generic structural damping ratio
μ	mean value
ν	kinematic viscosity
n	the frequency in Hz $\omega/(2\pi)$

1. Introduction

Computational Fluid Dynamics (CFD) simulations of the turbulent flows are commonly used in civil engineering to predict the actions and the effects of wind on structures.

Direct Numerical Simulation (DNS) or Large Eddy Simulation (LES) are the best numerical approaches to predict flow transition [1] , though they require great computational resources. A largely used alternative in the mechanical and civil engineering fields is represented by the Reynolds Average Navier-Stokes (RANS) equations [2-6]. However, these are not always reliable because they assume a fully turbulent regime and for this reason, they are not indistinctly suitable for all cases.

Locally-formulated RANS transition models have been developed in recent years in order to obtain numerical computations in an acceptable wall clock time. They can be divided into two main classes: local correlation-based transition models (LCTM) introduced in [7-8] and eddy viscosity phenomenological transition models [9] .

The main drawback of LCTM methods, also named $\gamma - R_{\widetilde{\theta},t}$ models, is in the adoption of empirical correlations that are not applicable for certain kinds of problems, whereas the $k - k_L - \omega$ technique has not always produced satisfactory results in flow cases characterized by large pressure gradient [10] . It should be noted that$\gamma - R_{\widetilde{\theta},t}$ models were initially coupled with the SST $k - \omega$ turbulence model by its developers, but the $\gamma - R_{\widetilde{\theta},t}$ model can be applied to other models too. In [12] the LCTM approach was coupled with the Spalart-Allmaras (SA) model to reduce the computational cost with respect to the SST $k - \omega$ model and the results were very satisfactory in the computation of external flows [13-14]. However, the SA transitional model was benchmarked against flow over aerodynamic bodies while bluff body flows have yet to be investigated in open literature.

Indeed, in literature we can find several references aimed in the analysis of the flow over bluff bodies based on standard fully turbulent models, [4-5] or experimental approaches, [6] , in particular in the mechanical science and mechanical engineering field.

D'Alessandro *et al*. [12] have discussed the Spalart-Allmaras (SA) local correlation based transition model for Reynolds Averaged Navier-Stokes (RANS) equation (i.e. in the following $\gamma - R_{\widetilde{\theta},t} - SA$ approach) performances. In particular, they investigated results obtained by this model on an air foil and they showed that this model gives an optimal prediction in the air foil stall regions.

Based on these satisfactory results, the same model was applied to predict the aerodynamics of sections with edges that produce massive flow separations. In particular, this paper is aimed at assessing the$\gamma - R_{\widetilde{\theta},t} - SA$ approach performances for computational fluid dynamic simulations of the flow streamlines around a closed box section of a suspended bridge that exhibits sharp corners in the transversal section.

The $\gamma - R_{\theta,t} \simeq SA$model reliability was proved comparing numerical and experimental results in regards to pressure coefficients and aerodynamic forces(i.e. drag, lift and moment coefficients). In addition, a suspended pedestrian bridge was assumed as case of study and its structure was sized using both, numerical and experimental dataset given by [15]. Finally, the natural frequencies and the preliminary critical flutter velocity were used as a measure of comparison. Two numerical models were used to compare experimental data, the traditional *SA – fully turbulent* model and the investigated $\gamma - R_{\theta,t} \simeq SA$ model.

The flutter instability analyses were carried out by a FE model and by the 2DOF Scanlan's approach 0. In both cases, the flutter derivatives were estimated according to the quasi-static approach given by Scalan and Tomko 0. It is important to specify that the flutter critical velocity estimated on a 2DOF model has to be considered a preliminary investigation of the bridge instability and that the quasi-static theory was applied considering the low reduced frequency of the case of study [15].

In Section 2, the governing equations of the Spalart-Allmaras (SA) local correlation based transition model for Reynolds Averaged Navier-Stokes (RANS) equations are given in. The numerical simulations set up is discussed in Section 3, while the main results of numerical simulations are discussed in Section 4. Experimental results are summarized in Section 5. The comparison between experimental and numerical results in terms of pressure coefficients and aerodynamic coefficients are discussed in section 6. Finally, the flutter critical speed estimated by both experimental and numerical data sets are discussed in Section 7.

1. Governing equations for fluid mechanics

The complete set of our flow governing equations, largely discussed in D'Alessandro *et al.* [12] , can be written as follows:

$$\begin{gathered} \nabla \cdot (u) = 0 \\ \frac{\partial u}{\partial t} + \nabla \cdot (u \otimes u) = -\nabla p + \nabla \cdot [(\nu + \nu_T)(\nabla u + \nabla u^T)] \\ \frac{\partial \tilde{\nu}}{\partial t} + \nabla \cdot (u\tilde{\nu}) = P_{\tilde{\nu}} - D_{\tilde{\nu}} + \frac{c_{b_2}}{\sigma} \nabla\tilde{\nu} \cdot \nabla\tilde{\nu} + \frac{1}{\sigma} \nabla \cdot [(\nu + \tilde{\nu})\nabla\tilde{\nu}] \end{gathered} \tag{1}$$

Where u is the velocity vector, $p = P/\rho$ is the pressure divided by the density and d is the distance from the nearest wall; while ν is the kinematic viscosity.

The turbulent viscosity, ν_T, needed to take into account the turbulence, is computed according to the ν_T variable as

$$\nu_T = f_{v1}\tilde{\nu} \tag{2}$$

The production and destruction terms appearing in the $\tilde{\nu}$ transport equation are defined as follows:

$$\begin{aligned} P_{\tilde{\nu}} &= \gamma_{eff} c_{b_1} \tilde{S}\tilde{\nu} \\ D_{\tilde{\nu}} &= max\big(min(\gamma, 0.5)\big)\left[c_{w_1} f_w \left(\frac{\tilde{\nu}}{d}\right)^2\right] \end{aligned} \tag{3}$$

The term γ_{eff} in Eq. 3 is a term devoted to model the separation-induced transition and it is defined as follows:

$$\gamma_{eff} = max\big(\gamma, \gamma_{sep}\big) \tag{4}$$

with

$$\gamma_{sep} = max\left(2.0 \cdot max\left(0, \left(\frac{R_v}{3.235 R_{\theta,c}}\right) - 1\right) F_{reattach}, 2.0\right) F_{\theta,t} \tag{5}$$

and

$$F_{reattach} = exp\left(\frac{-R_T}{20}\right)^4 \tag{6}$$

The following closure functions are now introduced to complete the definition of the SA equation given in Eq. 1:

$$\begin{aligned} f_{v1} &= \frac{\chi^3}{\chi^3 + c_{v_1}^3} & f_{v2} &= 1 - \frac{\chi}{(1 + \chi f_{v1})} \\ g &= r + c_{w_2}(r^6 - r) & f_w &= g\left(\frac{1 + c_{w3}^6}{g^6 + c_{w3}^6}\right)^{\frac{1}{6}} \\ \tilde{S} &= [\Omega + min\,(0, S - \Omega)] + \frac{\tilde{\nu}}{k^2 d^2} f_{v2} & r &= \begin{cases} r_{max} & \frac{\tilde{\nu}}{\tilde{S}k^2d^2} < 0 \\ min\left(\frac{\tilde{\nu}}{\tilde{S}k^2d^2}, r_{max}\right) & \frac{\tilde{\nu}}{\tilde{S}k^2d^2} \geq 0 \end{cases} \end{aligned} \tag{7}$$

Where $\chi = \tilde{\nu}/\nu$ is the dimensionless turbulent variable, $\Omega = \sqrt{2W\!:\!W}$ is the vorticity tensor module, $S = \sqrt{2D\!:\!D}$ is the strain rate tensor module and $\tilde{S}$ is a function of both vorticity magnitude, S , and $\tilde{\nu}$. The r_{max} is a constant positive value typically set at 10. The standard adopted closure constants are

$$c_{b_1} = 0.1355 \qquad c_{b_2} = 0.622 \qquad c_{v_1} = 7.1 \tag{8}$$

$$\sigma = 2/3 \qquad c_{w_1} = \frac{c_{b_1}}{k^2} + \frac{\left(1 + c_{b_2}\right)}{\sigma} \tag{9}$$

$$c_{w_2} = 0.3 \qquad c_{w_3} = 2.0 \qquad k = 0.41 \tag{10}$$

The transport equations needed to model the transition are:

$$\frac{\partial \gamma}{\partial t} + \nabla \cdot (u\gamma) = P_\gamma - D_\gamma + \nabla \cdot \left[\left(\nu + \frac{\nu_T}{\sigma_f}\right)\nabla\gamma\right]$$
$$\frac{\partial \tilde{R}_{\theta,t}}{\partial t} + \nabla \cdot \left(u\tilde{R}_{\theta,t}\right) = P_{\theta,t} + \frac{1}{\sigma}\nabla \cdot \left[\sigma_{\theta,t}(\nu + \nu_T)\nabla \tilde{R}_{\theta,t}\right] \tag{11}$$

The source terms in the γ equation are defined as:

$$P_\gamma = c_{a_1} S(\gamma F_{onset})^{0.5}\left(1 - c_{e_1}\gamma\right)F_{length}$$
$$D_\gamma = c_{a_2}\Omega\gamma F_{turb}\left(c_{e_2}\gamma - 1\right) \tag{12}$$

In P_γ the term F_{onset} is computed as:

$$F_{onset} = max\left(F_{onset,2} - F_{onset,3}, 0\right) \tag{13}$$

with

$$F_{onset,2} = min\left(max\left(F_{onset,1}, F_{onset,1}^4\right), 4.0\right)$$
$$F_{onset,3} = max\left(2 - \left(\frac{R_T}{2.5}\right)^3, 0\right) \tag{14}$$
$$F_{onset,1} = \frac{R_\nu}{2.193 R_{\theta,c}}$$

In Eq. 14 the terms R_ν and R_T are obtained as follows:

$$R_\nu = \frac{Sd^2}{\nu} \qquad R_T = \frac{\nu_T}{\nu} \tag{15}$$

The $R_T$parameter is redefined because, for k- ω model, it requires the estimation of ω. The definition based on the viscosity ratio enables the SA equation to be adopted. The aspects concerning the terms F_{length} and $R_{\theta,c}$ are described in the following. The coefficient F_{turb} is defined as:

$$F_{turb} = exp\left(\frac{-R_T}{4}\right)^{4} \tag{16}$$

As for the source terms in the transport equation for $\tilde{R}_{\theta,t}$, $P_{\theta,t}$, the following equation is adopted:

$$P_{\theta,t} = \frac{c_{\theta,t}}{T}\left(R_{\theta,t} - \tilde{R}_{\theta,t}\right)\left(1 - F_{\theta,t}\right) \tag{17}$$

In Eq. 17 the last term $F_{\theta,t}$ is defined as follows:

$$F_{\theta,t} = min\left(max\left(exp\left(\frac{-|u|^2}{375\Omega \widetilde{R_{\theta,t}}}\right)^4, 1-\left(\frac{\gamma - 1/c_{e_2}}{1-1/c_{e_2}}\right)^2\right), 1.0\right) \tag{18}$$

The term T appearing in the source term of the $\widetilde{R_{\theta,t}}$, equation is also defined as follows: $500\,\nu/|u|^2$. Finally, the computation of $R_{\theta,t}$ in Eq. 15 is discussed, together with the F_{length} coefficient, in the following.

For the turbulence model, the following closure constants were adopted in order to close Eq. 11

$$c_{a_1} = 2.0 \qquad c_{a_2} = 0.06 \qquad c_{e_1} = 1.0 \tag{19}$$

$$c_{e_3} = 50.0 \qquad c_{\theta,t} = 0.03 \qquad \sigma_f = 1.0 \tag{20}$$

$$\sigma_{\theta,t} = 2.0 \tag{21}$$

According to$\gamma - \widetilde{R_{\theta,t}}$ approaches available in literature [10-11], the present model contains three empirical correlations needed to compute $R_{\theta,t}$, $R_{\theta,c}$ and F_{length}. $R_{\theta,c}$, which appears in Eq. 14, where $R_{\theta,c}$ is the critical Reynolds number where the intermittency starts to increase in the boundary layer. This typically occurs upstream from the transition Reynolds number, $R_{\theta,t}$. This element relates to the delay from turbulence onset and the beginning of appreciable turbulence levels within the boundary layer. It is important to note that this last feature is essential to obtain a significant change in the laminar velocity profile. F_{length}, appearing in the production term of the transport equation, is an empirical correlation that controls the length of the transition region. In this paper, a correlation developed by [7] and [8] for $R_{\theta,t}$ was adopted:

$$R_{\theta,t} = \begin{cases} (1173.51 - 589.428 \cdot Tu + 0.2196 \cdot Tu^2)F(\lambda_\theta) Tu \leq 1.3 \\ 331.5(Tu - 0.5668)^{-0.671} F(\lambda_\theta) Tu > 1.3 \end{cases}$$

$$F(\lambda_\theta) = \begin{cases} 1 - \left[12.986\lambda_\theta + 123.66 \cdot \lambda_\theta^2 + 405.689 \cdot \lambda_\theta^3\right] exp\left(-\left(\frac{Tu}{1.5}\right)^{1.5}\right)\lambda_\theta \leq 0 \\ 1 + 0.275[1 - exp\,(-35\lambda_\theta)] exp\left(\frac{-Tu}{0.5}\right)\lambda_\theta > 0 \end{cases} \tag{22}$$

The correlations in Eqs. 21 and 22 contain turbulence intensity Tu. In the framework of the k-ω model, Tu can be computed using the solution for k equation.

In this work, the approach introduced by [25] was adopted and specifically, we established $Tu = Tu_\infty$ for all the points of the flow field. Moreover $R_{\theta,t}$was computed by iterating on the value of θ_t, since $R_{\theta,t}$ is a function of θ itself because of the presence of λ_θ. Differently for $R_{\theta,c}$ and F_{length}we used the correlations introduced by [17] :

$$R_{\theta,c} = min\left(0.615R_{\widetilde{\theta},t} + 61.5, R_{\widetilde{\theta},t}\right) \tag{23}$$
$$F_{length} = min\left(exp\left(7.168 - 0.01173R_{\widetilde{\theta},t}\right) + 0.5{,}300\right)$$

2. Grid generation and boundary conditions

Boundary conditions were adopted for $\tilde{\nu} = 3\nu$ at the free stream and $\tilde{\nu} = 0$ at the wall, while the boundary condition for γ at the wall is zero normal flux. At the inlet, the value of γ is 1. The boundary condition for $R_{\widetilde{\theta},t}$ at the wall is zero flux, while at the inlet $R_{\widetilde{\theta},t}$was calculated from the specific empirical correlation based on the inlet turbulence intensity. It is also very important to note that, in order to capture the laminar and transitional boundary layers correctly, the grid has a viscous sub-layer scaled first cell height, y^+, of approximately 1. The value of y^+ is estimated as $y^{+u_\tau y_p/\nu}$, where $u_\tau = \sqrt{\tau_w/\rho}$is the friction velocity, τ_w is the viscous stress component measured at the wall, and y_p is the height of the cells next to the wall.

The numerical model was applied to a closed box section of a suspended pedestrian bridge 0characterized by the geometry illustrated in Fig.1 and summarized in Table 1. It is important to note that this geometry was chosen because it is very similar to geometries discussed in literature [21-23]. The numerical simulations were computed on a 2D O-type domain and the far-field was placed at about 18 times the chord length as is illustrated in Fig.2a. A fully structured grid having 317934 grid cells with elements clustering near the walls was employed, as in Fig.2b.

It is important to note that in this study the cross section equipment was neglected although it is known that these affect the cross section aerodynamics [21-23] in order to compare numerical results with experimental data set.

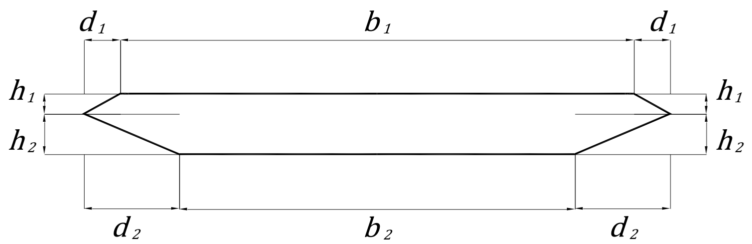

Fig. 1 Bridge closed deck section geometrical parameters. Measures are given in Table 1 for the full scale bridge, the section wind tunnel model and the numerical model.

Table 1

Main geometric properties of the full-scale deck girders, wind tunnel section models and CFD numerical model, measures in meters.

	h_1	h_2	d_1	b_1	d_2	b_2
Full scale	0.53	1.11	0.94	10.25	1.89	8.36
Wind tunnel model scale $(\cdot 10^{-3})$	13	27	21	250	46	204
CFD model scale	0.53	1.11	0.94	10.25	1.89	8.36

Governing equations were solved by means of simpleFoam which is a steady solver for incompressible flows available in the official releases of the OpenFOAM (Open-source Field Operation and Manipulation). The collocated unstructured finite volume method available within OpenFOAM was adopted for the space discretization; in particular, simpleFoam uses the well-established SIMPLE algorithm [18] for pressure-velocity decoupling. On the other hand, Rhie-Chow correction was used to remove oscillations in the solutions [19] , [22]. For all the computations presented in this paper, the diffusive terms and pressure gradients were approximated with second-order accurate central schemes. The convective terms for momentum and turbulence equations were handled with a second order accurate linear-upwind scheme. For the linear solvers a preconditioned bi-conjugate gradient method (PBiCG) with the DILU preconditioner was used to solve the discretized momentum, γ and $R_{\widetilde{\theta},t}$ equations.

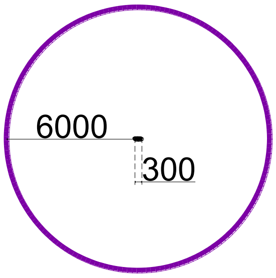

(a) Computational fluid dynamics circular 2D domain size measures in m.

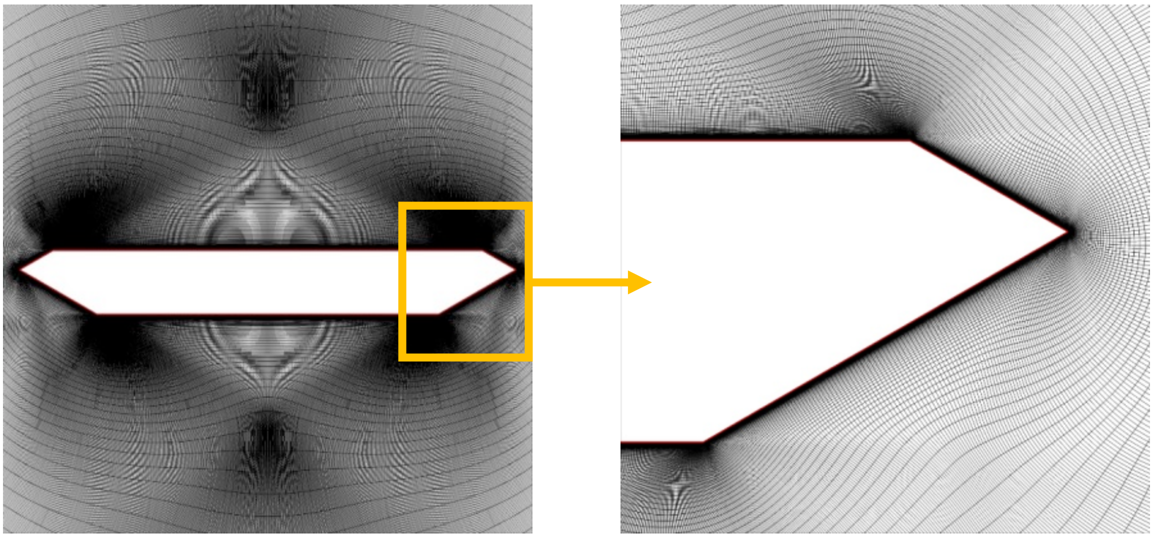

(b) Computational fluid dynamics grid cells distribution with a focus around the edges.

Fig. 4 Two-dimensional numerical domain for computational fluids dynamic simulations. The sizes and the adaptive mesh distribution are shown.

A preconditioned conjugate gradient method (PCG) with a diagonal incomplete-Cholesky preconditioner was adopted instead for the pressure. In particular, a local accuracy of 10^{-7} was established for the pressure, whereas other linear systems were considered converged when the residuals reached the machine precision [23].

3. Results and discussions

Numerical simulations were carried out for several angles of attack ranging from α=-10° to 10 in order to test the reliability of the adopted turbulence modeling approaches compared with experimental data. Simulations were carried out using a wind speed equal to 8.5 m/s. The Reynolds number is equal to $1.76 \cdot 10^5$, estimated using the kinematic air viscosity equal to $1.45 \cdot 10^{-5}$.

Figures 3 and 4 show the stream-wise velocity at α between -10° to 0° and from 2° to 10°, respectively. The figures show a very different pattern of the flow streamlines distribution around the box section for the two turbulence models. It is noted that the SA - fully turbulent model(Figs. 3a and 3b)completely removes the separation bubble predicted by the LCTM version of the SA model (i.e. $\gamma - R_{\widetilde{\theta},t}$-SA). Besides, a zone with almost a constant pressure coefficient can be noted in the C_p distributions for the $\gamma - R_{\widetilde{\theta},t}$-SA approach, Figs. 3b and 4b. This is due to the standard SA approach inability in the prediction of the laminar-to-turbulent transition occurring in the separated shear layer. Fig.3 shows that the two numerical approaches give a significant difference at α greater than -6°, for which $\gamma - R_{\widetilde{\theta},t}$-SA calculates a larger separation in the detachment zones than *SA – fully turbulent*. This is particularly evident at α equal to 0°. In fact, at this angle, dot lines show that $\gamma - R_{\widetilde{\theta},t}$-SA estimates the peak of the separation downstream from the corner better than *SA – fully turbulent*. This is in agreement with experimental results discussed in Section 5. Similarly, for α greater than 0° (Fig.4) $\gamma - R_{\widetilde{\theta},t}$-SA show a different trend of the streamlines in particular at the lower surface close to the detachment zone. Fig.4, for α= 6°, shows that at the upper surface, the streamlines given by $\gamma - R_{\widetilde{\theta},t}$-SA are extended for all the sloped side length (i.e. zone marked by a dot line in Fig.4). Contrarily, the streamlines given by SA – *fully turbulent* show a reattachment at 2/3 of the sloped side that seems unrealistic. Fig.5 shows the numerical solution of the vorticity (i.e. the velocity curl of the velocity $\vec{u}$ vector in direction z, Fig.2) at α=-10° to 10° computed through SA – *fully turbulent* (Fig.5a) and through $\gamma - R_{\widetilde{\theta},t}$-SA approach (Fig.5b), respectively. Fig.5 shows some significant differences between the two models; in particular, the differences are evident for positive angles as for example α = 10°. The $\gamma - R_{\widetilde{\theta},t}$-SA reduces the tendency by flow to be attached on the surfaces. This is evident in Fig.5 for α=0° and 10° on the top and for α=-6° and -2° on the bottom of the deck.

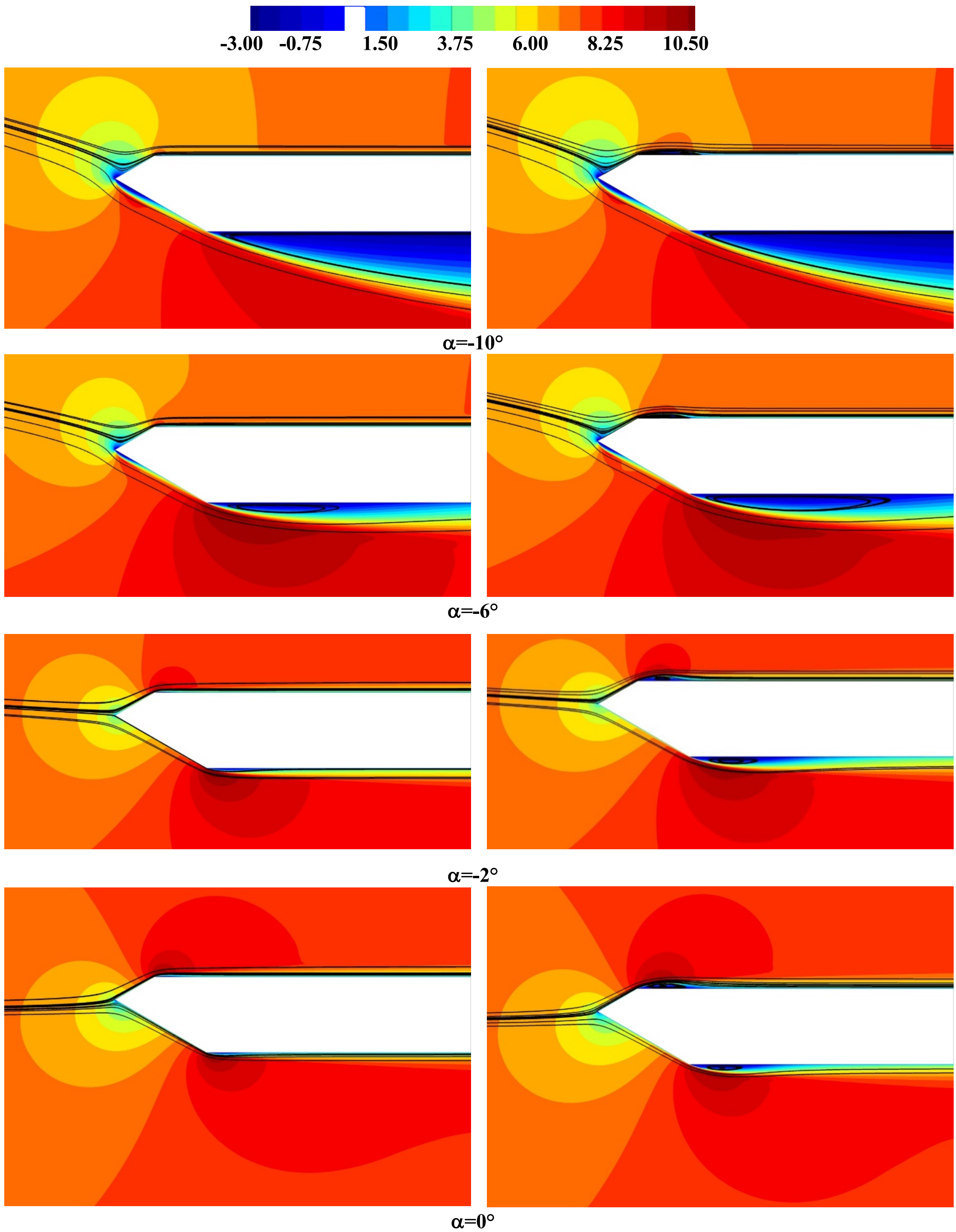

(a) Numerical solution contour plots stream-wise velocity at α from -10° to 0° by SA – fully turbulent approach.

(b) Numerical solution contour plots stream-wise velocity at α from -10° to 0° by $\gamma - R_{\tilde{\theta},t}$-SA approach.

Fig. 3 Numerical solution contour plots stream-wise velocity at α from -10° to 0° obtained by both SA – fully turbulent approach and $-R_{\tilde{\theta},t}$-SA approach are shown. Values range from -3 to 10.5 m/s.

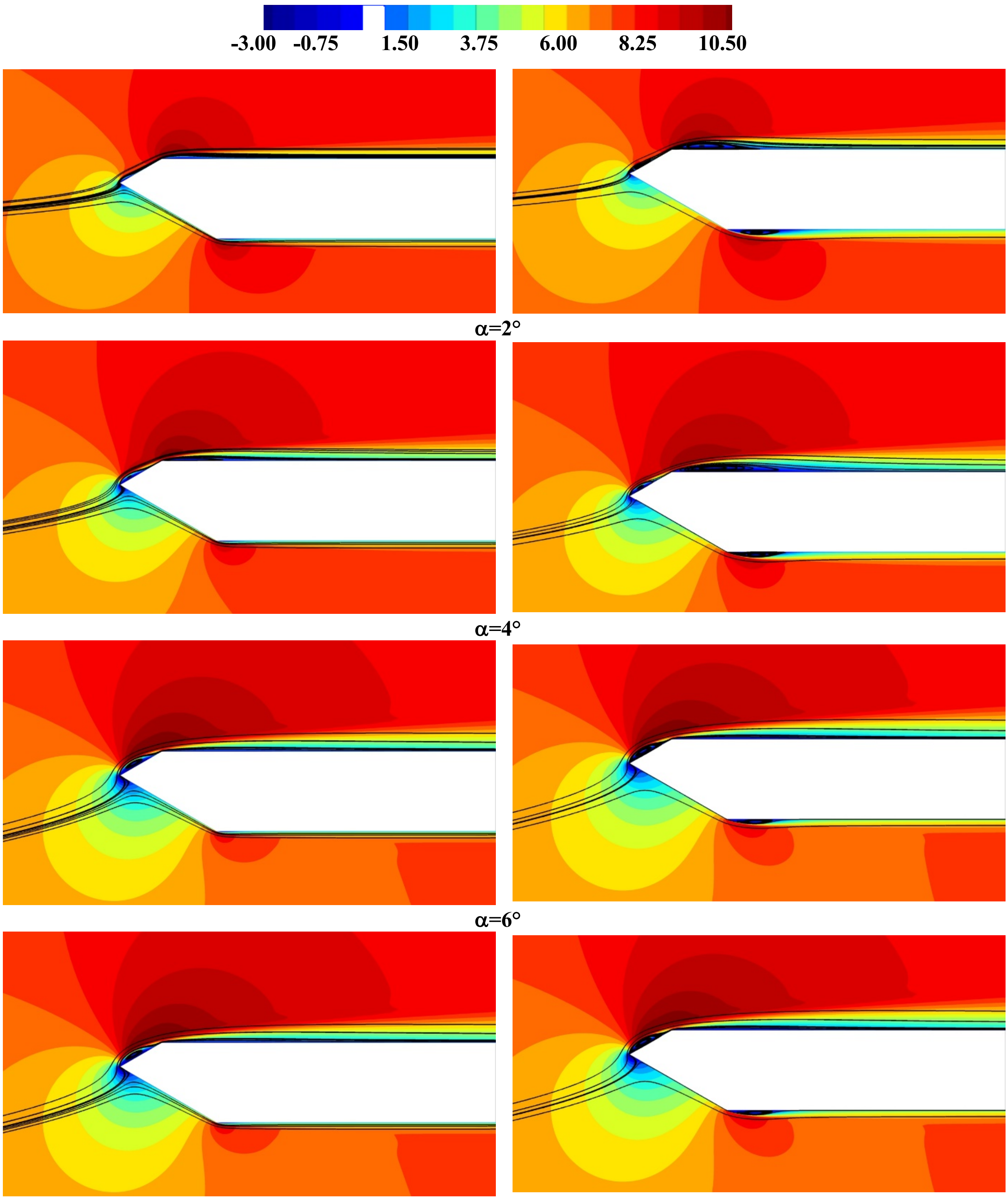

(a) Numerical solution contour plots stream-wise velocity at α from -10° to 0° by SA – fully turbulent approach

(b) Numerical solution contour plots stream-wise velocity at α from -10° to 0° by$\boldsymbol{\gamma - \tilde{R}_{\theta,t}}$-SA approach.

Fig. 4 Numerical solution contour plots stream-wise velocity at α from 2° to 10° obtained by both SA – fully turbulent approach and $\boldsymbol{-\tilde{R}_{\theta,t}}$-SA approach are shown. Values range from -3 to 10.5 m/s.

Finally, Figs.6 and 7 show the pressure contour plots at wind angles α between -10° to 0° (Fig.6) and between 2° to 10° (Fig.7). These maps confirm the differences between the two numerical approaches and in particular Fig.6 for α=-6°.

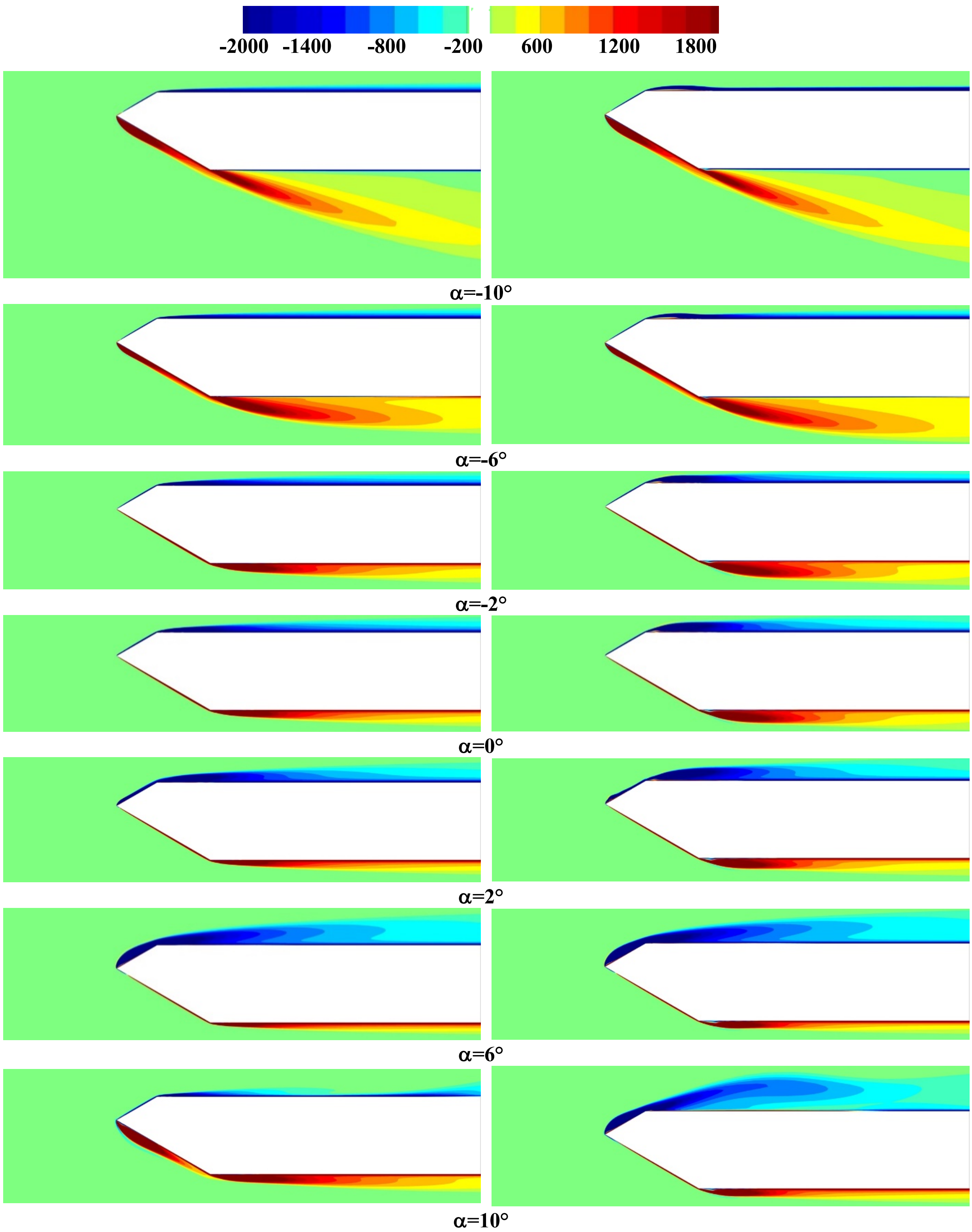

(a) Numerical solution contour plots vorticity at α=-10° to 10° by SA – fully turbulent approach.

(b) Numerical solution contour plots vorticity at α=-10° to 10° by $\boldsymbol{\gamma - R_{\tilde{\theta},t}}$-SA approach.

Fig. 5 Numerical solution contour plots vorticity at α=-10° to 10° obtained by both SA – fully turbulent approach and $\boldsymbol{-R_{\tilde{\theta},t}}$-SA approach are shown. Values range from -2000 to 1800 1/s. Measures in 1/s.

4. Experimental measurements

The pressure coefficients acquisition tests were carried out in the open-circuit CRIACIV boundary layer wind tunnel in Prato (Italy) featuring test chambers 2.42 m in width and 1.60 m in height, and an approximately 22 m long wind tunnel . The closed box test model was equipped with 40 pressure taps located all around its middle section [15]. Fig.8a shows a picture of the experimental setup.

(a) View of pressure tests at CRIACIV Boundary Layer Wind Tunnel lab.

(b) View of aerodynamic forces measurements at Polytechnic University Wind Tunnel.

Fig. 8 Experimental setup views of the two experimental campaign in wind tunnel on two rigid models. The pressure tests model pressure taps , the . The models are equipped with end plates.

Wind speed is regulated both by adjusting the pitch of the ten-fan blades and by controlling the angular speed of the motor ([24-30]). The models were horizontally placed in the wind tunnel with fixed connections composed of rigid arms, as illustrated in Fig. 2b. The pressure signal sampling frequency was 500 Hz and the acquisition time was 60 s. The inlet turbulence intensity had a mean value of about 1%. The standard deviations of speed and turbulence were between 0.1 and 0.2. In order to investigate the Reynolds number dependence, tests were repeated using three mean flow speeds U: 3.5, 8.5 and 14.5 m/s. Results did not show a significant dependence by Reynolds number. The blockage ratio was lower than 1% at α equal to 0° and 4% at α equal to -10°.

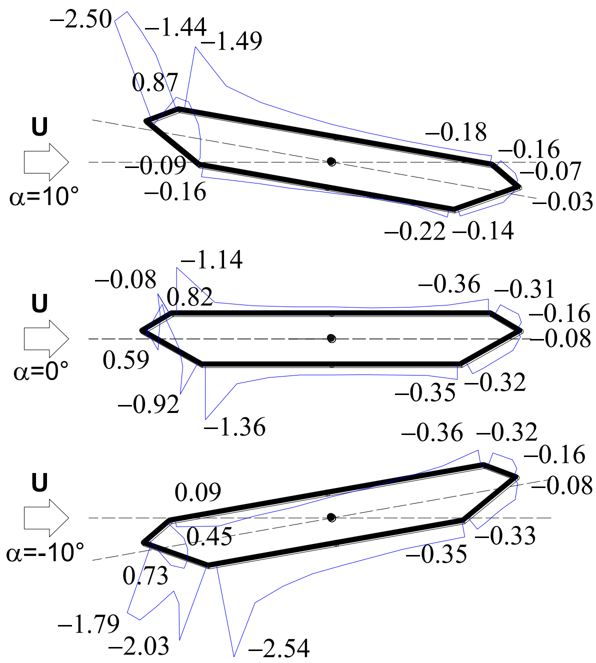

Fig. 9 Example of pressure coefficients distribution on the closed box section ([10]) for -10, 0 and 10 angles of attack. U means wind velocity and the arrow means the wind direction. Negative values mean suction and positive value mean pressure on the deck surface.

Corrections due to the blockage ratio were used to adjust the acquired raw pressure data [16]. Dimensionless pressure coefficients (C_p) were estimated from the difference relating to the static pressures measured at each pressure tap (p_i) and the reference flow static pressure p_0 [24], according to Eq. (24).

$$C_p = \frac{p_i - p_0}{\frac{1}{2}\rho U^2} \tag{24}$$

According to [31] the gaussianity of the pressure coefficients, time histories were investigated by $|\gamma_{cp}|$>0.5 and/or $|k_{cp}|$>0.5, where γ_{cp} is the skewness and k_{cp} is the excessive kurtosis of the process. It was assessed that all series can be considered a Gaussian process, and this is significant because it allows for a measure of the numerical approach (i.e. $\gamma - \widetilde{R}_{\theta,t}$-SA and *SA- fully turbulent*) reliability by evaluating the distance between experimental quantiles and numerical data [32].

Table 2

Pressure coefficients statistics

Surface	$C_{p,max}$	$C_{p,m}$	$C_{p,min}$	σ_{C_p}	γ_{cp}	k_{cp}	N (%)
Up Statistics on 21 pressure taps	0.01	-0.90	-3.00	0.04	-0.02	0.15	100
Down Statistics on 19 pressure taps	1.08	0.12	-0.43	0.03	-0.03	-0.22	100

Aerodynamic forces were measured in the closed circuit wind tunnel of the Marche Polytechnic University (Ancona, Italy) [15]. The cross-sectional test chamber is a square with side lengths measuring about 1.8 m. The wind tunnel is equipped with a fan having a constant rotational speed of 975 rpm and 16 blades with adjustable pitch. Fig. 8b shows a picture of the experimental setup. The load balance sampling frequency was equal to 500 Hz and the acquisition time was equal to 60 s. The purpose of these tests was to measure the aerodynamic force parallel to the flow, Drag (D), the aerodynamic force perpendicular to the flow, Lift (L) and the aerodynamic moment around the bridge longitudinal axis, Torsional Moment (M) of the deck, according to the reference system shown in Fig.4, and in order to estimate the Drag (C_D), Lift (C_L) and Torsional Moment (C_M) coefficients. These non-dimensional representations of the lift, drag and pitching moment allow one to compare two aerodynamic bodies of different size, shape, and orientation to one another having normalised the result to account for the variation in the force produced by the size of the body and the conditions of flow.

The tests were repeated using three mean flow speeds U: 3.5, 8.5 and 14.5 m to investigate the Reynolds number dependence: similarly, to the pressure tests, the results showed a non-significant dependence by Reynolds number.

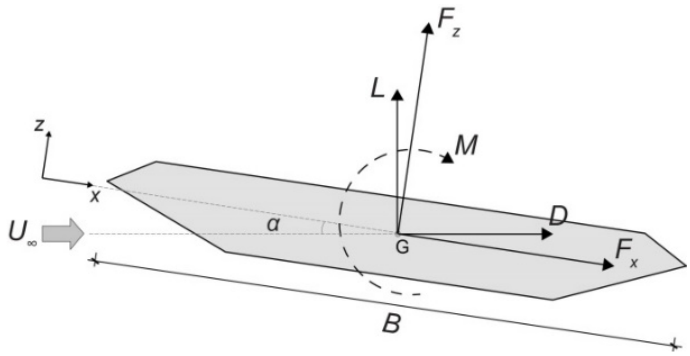

Fig. 10 Reference system for the calculation of the aerodynamic forces. *L* means Lift, *D* means Drag and *M* means Moment respect the center of gravity *G*; *B* is the deck chord, F_x and F_z are the drag and lift components in agreement with the *x-z* system of reference; $\boldsymbol{U}_\infty$ is the wind velocity according the direction shown by the arrow.

The average values of drag, lift and torsional moment coefficients, respectively C_D,C_L and C_M, were evaluated according to Eq. 25:

$$C_D = \frac{D}{\frac{1}{2}\rho U^2 BW}, C_L = \frac{L}{\frac{1}{2}\rho U^2 BW}, C_M = \frac{M}{\frac{1}{2}\rho U^2 \mathrm{B}^2 W} \quad (25)$$

In Eq. 25, U is the flow speed, ρ is equal to 1.18 kg/m^3 and, in Table 1, B is the reference length equal to $2d_1+b_1$= 298 mm and W is the experimental model length equal to 1 m. The model was placed vertically (Fig. 10b) and twenty-one values of the wind angle of attack (α) were considered in the interval between -10° and +10°: positive angles are "nose up", according to Fig.10.

5. Numerical and experimental data matching

5.1 Comparison with the experimental pressure distributions

The comparison between experimental and numerical results have shown that, $\gamma - R\widetilde{\theta,t}$-SA gives an appreciable and satisfactory prediction of experimental data as shown in Figures 11, 12 and 13.

Figures 11 and 12 show the experimental pressure coefficient trend and the error strip estimated as $C_{p,m,i} \mp \sigma_{C_{p,i}}$, where $C_{p,m,i}$ is the mean pressure coefficient for every pressure tap and $\sigma_{C_{p,i}}$ is the standard deviation of the pressure coefficient time history. In addition, based on results discussed in

Section 5 and summarized in Table 2, assuming a Gaussian distribution for pressure coefficients, the 5% quantile ($C_{p,\mathrm{k}}$, 5%) is overlapped to experimental data, and was estimated as $C_{p,m,i} \mp 1.64\sigma_{C_{p,i}}$. In order to measure the numerical simulation result reliability for each pressure tap, the number of numerical values inside the 5% experimental quantile was estimated. A percentage for all wind angles is summarized in Table 3. Table 3 shows a significant difference between $\gamma - R_{\widetilde{\theta},t}$-SA and *SA- fully turbulent* for the specific case of study investigated. In fact, for $\gamma - R_{\widetilde{\theta},t}$-SA the percentage in the upper surface is between 72.1% and 95.4%, with a mean value equal to 89.2%, and in the lower surface it ranges between 58.4% and 98.0%, with a mean value equal to 76.4%. Contrarily, for *SA-fully turbulent*, the percentage ranges from 65.8% to 92.2%, with a mean value equal to 78.9 % in the upper surface and from 26.3% to 91.0 %, with a mean value equal to 45.9%, in the lower one. It was noted that the percentage decreases from upper to lower surface and this is particularly evident for *SA- fully turbulent* approach. On average, the $\gamma - R_{\widetilde{\theta},t}$-SA approach is in the 5% experimental quantile for 83% of the numerical results.

The accuracy of the $\gamma - R_{\widetilde{\theta},t}$-SA approach is shown in Figures 11 and 12 where the pressure coefficients experimentally and numerically estimated for the upper and lower surface are compared. In particular, Figs.11 and 12 show a comparison at α equal to -4°, 0° and 4° that is a significant range around zero degree [24, 33]. A good agreement between experimental and numerical data in this range gives a satisfactory agreement of flutter derivatives estimated by the quasi-static method.

Table 3

Percentage of numerical values inside the experimental 5% quantile.

	Up		Down	
α	$\gamma - R_{\widetilde{\theta},t}$-SA	*SA- fully turbulent*	$\gamma - R_{\widetilde{\theta},t}$-SA	*SA- fully turbulent*
-10°	95.3%	92.2%	59.1%	55.6%
-8°	89.8%	89.5%	58.4%	41.9%
-6°	92.9%	86.9%	59.7%	32.1%
-4°	94.8%	84.2%	64.9%	26.3%
-2°	95.4%	81.6%	70.2%	24.3%
0°	94.7%	79.0%	75.4%	26.3%
2°	92.8%	76.3%	80.7%	32.2%
4°	89.5%	73.7%	86.0%	42.0%
6°	85.0%	71.0%	91.2%	55.8%
8°	79.2%	68.4%	96.5%	73.4%

10°	72.1%	65.8%	98.0%	91.0%

Fig.12 shows that $\gamma - R_{\widetilde{\theta},t}$-SA exhibits the best prediction in regards to experimental behavior, in particular in the detachment zone where the differences between $\gamma - R_{\widetilde{\theta},t}$-SA and *SA-fully turbulent* are more evident; an exception has to be underlined for α= 4°,where both models are quite distant from the experimental curve, although the$\gamma - R_{\widetilde{\theta},t}$-SA is slightly better than the other. For the lower surface, the trend is similar to the upper one; in particular, the $\gamma - R_{\widetilde{\theta},t}$-SA approach gives a better approximation of the higher-pressure coefficient values.

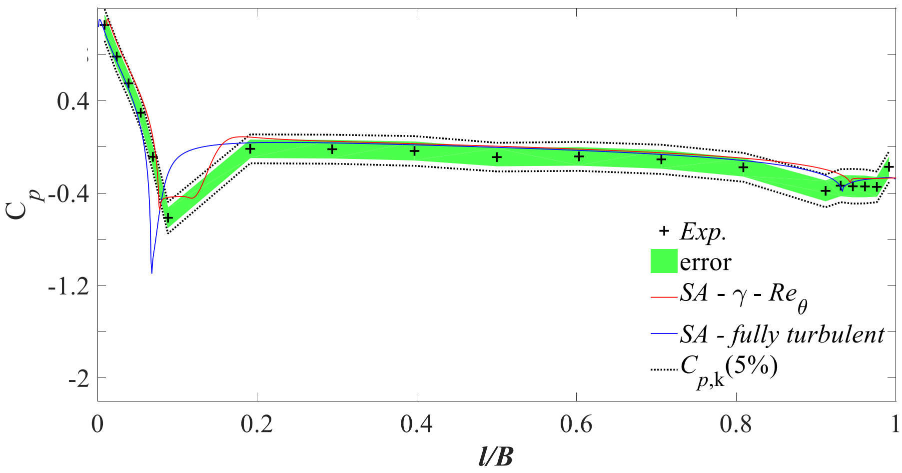

(a) Comparison between experimental and numerical pressure coefficients on the upper surface at α = -4°

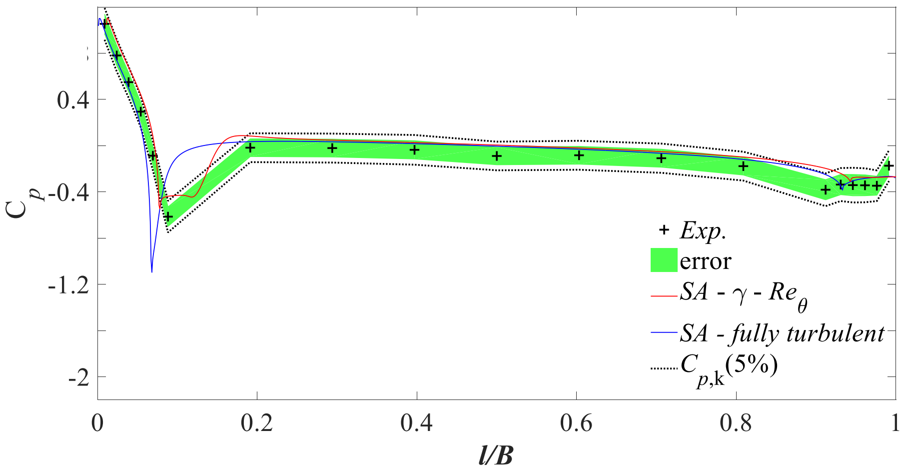

(b) Comparison between experimental and numerical pressure coefficients on the upper surface at α = 0°

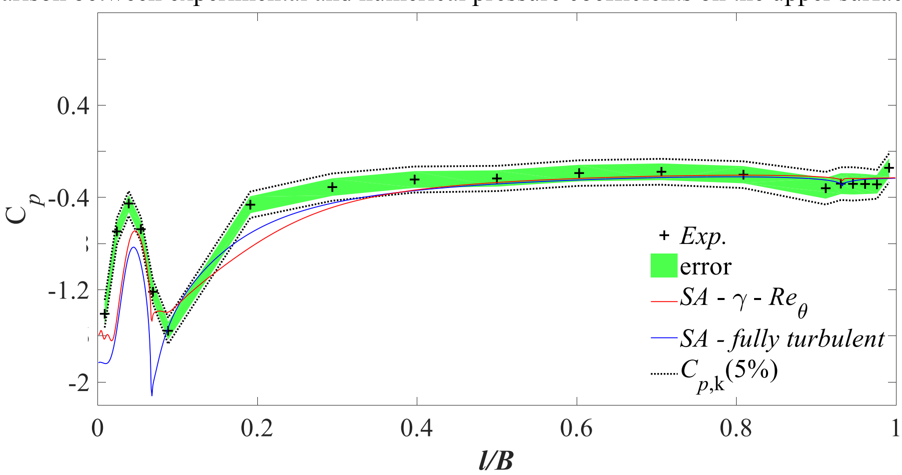

(c) Comparison between experimental and numerical pressure coefficients on the upper surface at α = 4°

Fig. 11. Pressure coefficients distribution on the upper surface for angles of attack equal to -4°, 0° and 4°. Results given by the $\boldsymbol{\gamma - R_{\tilde{\theta},t}}$-SA and the SA – fully turbulent models are compared with experimental results and the 95% level of confidence of the experimental data. The error strip means the 95% level of confidence.

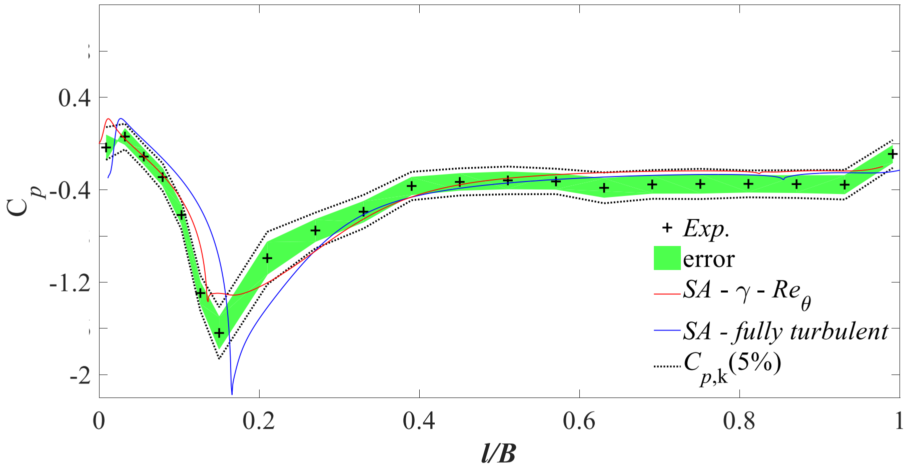

(a) Comparison between experimental and numerical pressure coefficients on the bottom surface at α = -4°

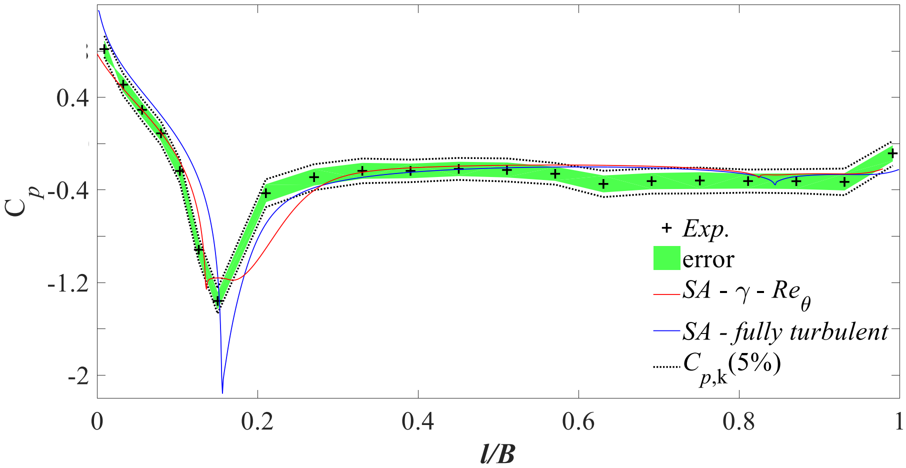

(b) Comparison between experimental and numerical pressure coefficients on the bottom surface at α = 0°

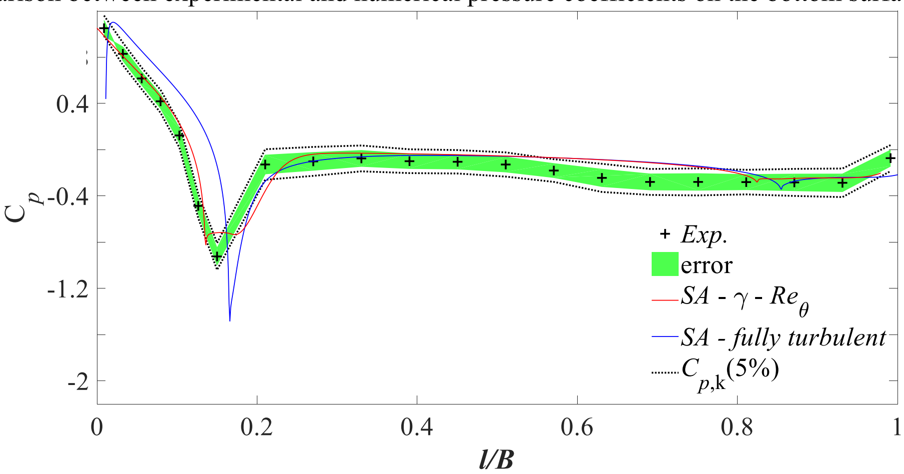

(c) Comparison between experimental and numerical pressure coefficients on the bottom surface at α = 4°

Fig. 12 Pressure coefficients distribution on the bottom surface for angles of attack equal to -4°, 0° and 4°. Results given by the $\boldsymbol{\gamma - R\tilde{e}_{\theta,t}}$-SA and the SA – fully turbulent models are compared with experimental results and the 95% level of confidence of the experimental data. The error strip means the 95% level of confidence.

Contrarily, the SA-*fully turbulent* approach overestimates pressure coefficients in the maximum suction peak zone. Finally, at α equal to 0° (Figs.11b and 12b) the $\gamma - R\tilde{e}_{\theta,t}$-SA approach gives a very precise approximation of the experimental data. Globally, the differences between the two numerical approaches are significant and they induce a structural sizing variability as will be discussed in Section 7.

5.2 Comparison with the experimental aerodynamic coefficient distributions

A comparison between experimental and numerical coefficients is shown in Fig.13. The experimental aerodynamic coefficients were calculated using both pressure and load balance static tests described in Section 5. The uncertainty given by the standard deviation (i.e. interval of confidence of 95% assuming a Gaussian distribution) of the experimental forces time histories acquired in wind tunnel with pressure tests (P) is also reported [15, 24, 33]. The comparison between experimental and numerical models shows that $\gamma - R_{\widetilde{\theta},t}$-SA is closer to the experimental values than *SA-fully turbulent.* Fig.13 shows that the $\gamma - R_{\widetilde{\theta},t}$-SA approach trend is between experimental coefficients obtained by pressure and static tests. This is particularly evident for α in the range between -10° to -6° and 6° to 10°. In the range around zero (i.e. for α from-4 to 4°) the two models are very close even if the $\gamma - R_{\widetilde{\theta},t}$-SA is slightly closer to experimental values than the other is. In particular, the numerical values estimated by $the\gamma - R_{\widetilde{\theta},t}$-SA approach are very close or often they are inside the error band of the aerodynamic coefficients estimated by pressure tests. Contrarily, values estimated by the *SA-fully turbulent* approach are not satisfactorily close enough to experimental results, especially concerning higher negative and positive angles of attack. However, both methods give a satisfactory approximation of the experimental data around zero. This is a very important result because it means that the numerically estimated aerodynamic coefficients shall give a good approximation of flutter derivatives following the quasi-static approach [24, 34].

The global forces coefficient trend confirms once again the goodness of the $\gamma - R_{\widetilde{\theta},t}$-SA numerical approach for the section assumed as case of study.

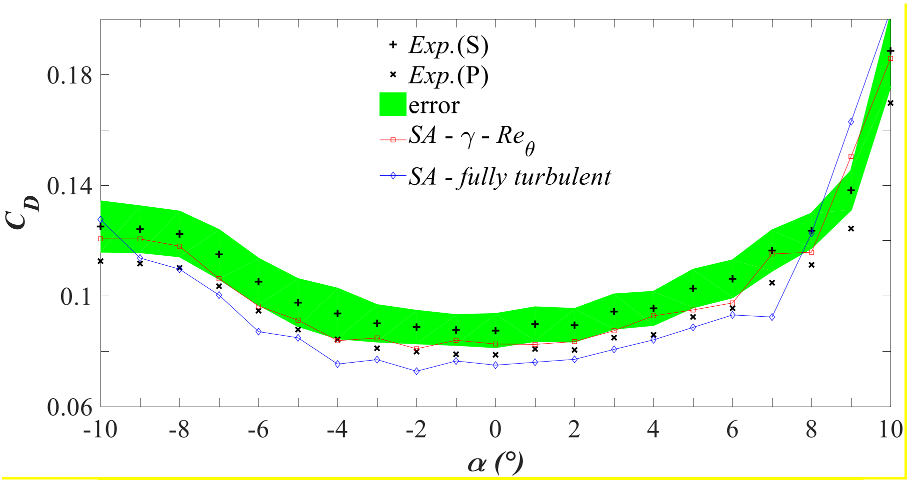

(a) Comparison between experimental and numerical Drag coefficient.

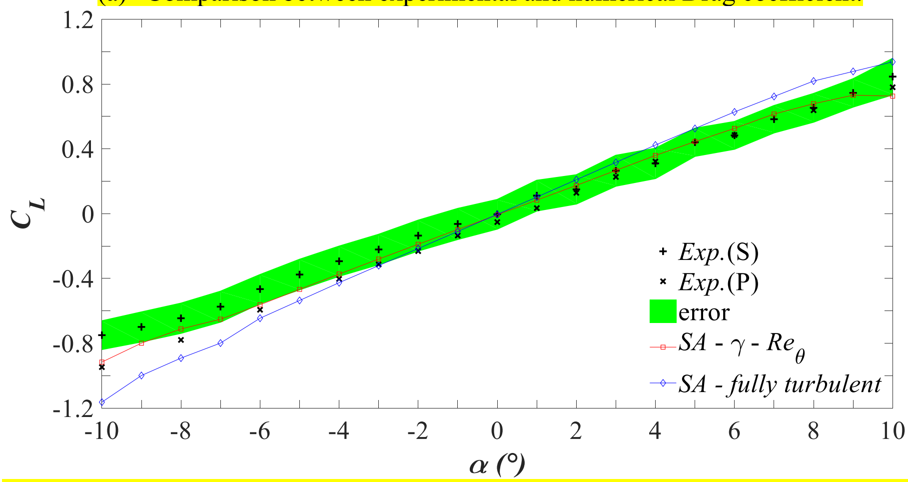

(b) Comparison between experimental and numerical Lift coefficient.

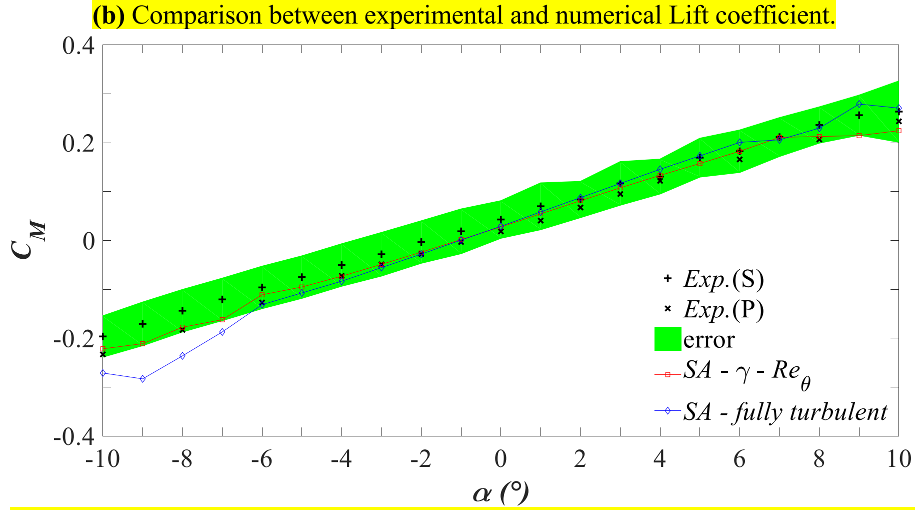

(c) Comparison between experimental and numerical Moment coefficient.

Fig. 13 Aerodynamic coefficients of drag, C_D, lift, C_L and moment, C_M, are shown. The 95% level of confidence of values estimated from experiments is compared with values given by the $\boldsymbol{\gamma - \tilde{R}_{\theta,t}}$-SA and the SA – fully turbulent models.

In the following section, the incidence of the numerical method differences on the critical flutter speed as a measure of the numerical approach reliability will be exploited [35-38]. The case study of a suspended pedestrian bridge made of steel given by 0was taken as reference and designed according to [39].

6. Sensitive structural analyses

7.1 Structural design

The three sets of pressure coefficients data (i.e. by experimental, $\gamma - R_{\widetilde{\theta},t}$-SA and by SA-fully turbulent numerical approaches) were used to size the section deck and the structure of the towers of a pedestrian bridge assumed as case study [15]. The aim was to show the differences in terms of structural performances due to the different three pressure input data sets as a preliminary design of a suspended pedestrian bridge. Fig. 14a shows the geometry of the case of study investigated. H_1 and H_2 are respectively equal to 45 m and 15 m; L_1, L_2 and L_3 are equal to 494 m, 584 m and 45 m, respectively. Finally, f is equal to 3 m. The center-to-center distance between the two main suspension cables is about 10 m.

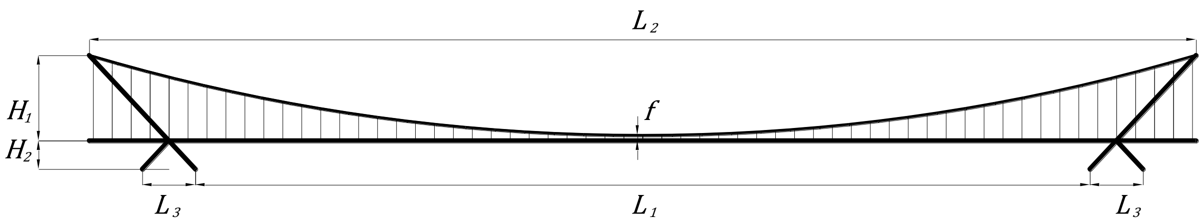

(a) Bridge structure geometrical parameters overview.

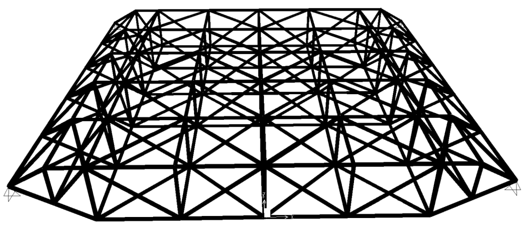

(b) View of the FE local model of the deck structure.

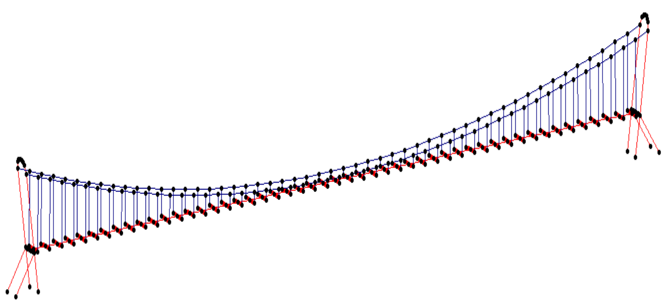

(c) View of the FE global model of the bridge structure.

Fig. 14 The global geometry of the bridge is shown. H_1 and H_2 are respectively equal to 45 m and 15 m; L_1, L_2 and L_3 are equal to 494 m, 584 m and 45 m, respectively. Finally, f is equal to 3 m. The center-to-center distance between the two main suspension cables is about 10 m. The local FEM model of the deck and the global FEM model of the bridge used to compute the bridge structural response are shown.

The selected design simulates a deck structure built by hollow-structural steel pipes (Fig.14b). A wood deck surface and a thin sheet metal coating were used to simulate the deck superstructure. Finite Element (FE) analyses on a FE model (Fig.14c) were performed to design the bridge structure 0, [38] using the pressure coefficients to evaluate the wind actions; all the calculations were carried out according to [39] . The steel elements (i.e. fy = 275 MPa) were modelled using truss finite elements whereas cables (i.e. fy = 1100 MPa) were modelled using the rectilinear cable finite element. Geometric non-linear analyses were carried out using the noncommercial program TENSO 0 which enables non-linear dynamic analysis of wind-structure interaction at flutter. The bridge deck is simplified by a beam model located in the deck section’s center of gravity and two massless rigid links to simulate the connection of the deck to the hangers and cables. Modal analysis was carried out to estimate natural frequencies [15]. All calculations were performed using a structural damping ratio ζ equal to 0.3%. This value was preliminarily set knowing that the damping ratio closely affects the flutter critical speed value 0.

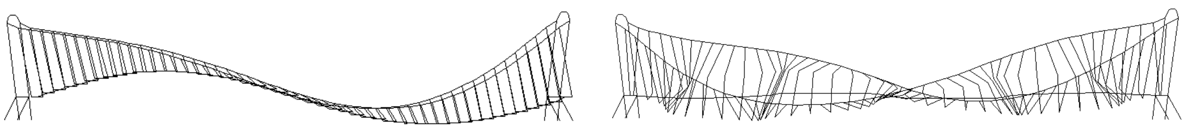

(a) Bridge 1th symmetric vertical mode shape **(b)** Bridge 1th symmetric torsional mode shape

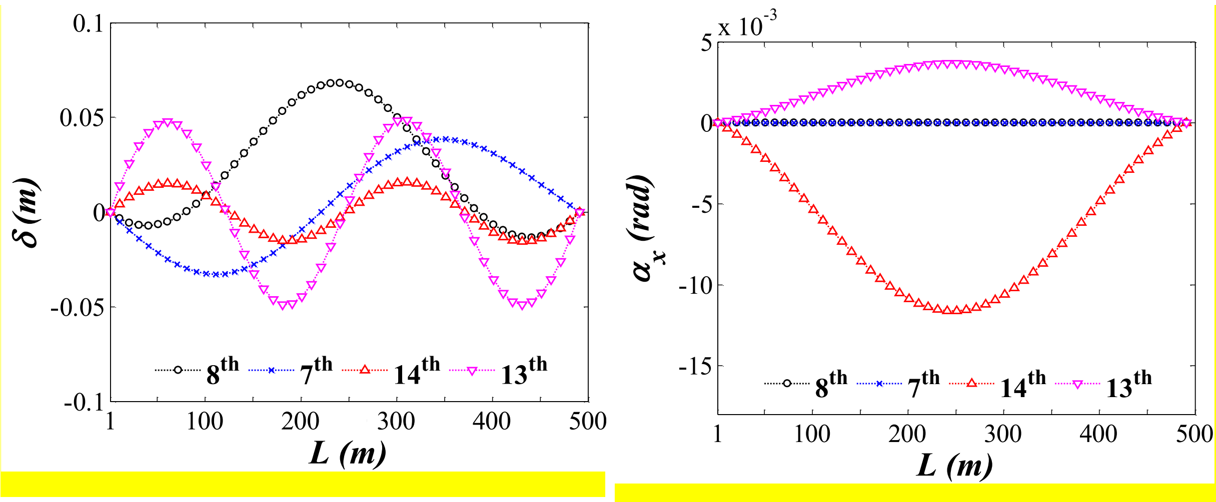

(c) Deck vertical displacements for significant modes. **(d)** Rotations of the deck about the longitudinal bridge axis (α_x) for significant modes.

Fig. 15 The 1^{th} symmetric vertical and torsional mode shapes are shown. It is shown the deck vertical displacements for the most significant modes (i.e. in term of participating mass ratio); modes respectively are #7, #8, #13 and #14.

It was estimated that the deck mass varies 759.42 kg/m using experimental values, 685.19 kg/m using $\gamma - R_{\widetilde{\theta},t}$-SA (-10%) and 1092.37 kg/m (+47%) using *SA-fully turbulent* approach. This mass variability is significant and spreads on the global bridge performance because it affects the natural structural frequencies. In fact, it was estimated that the first symmetrical vertical frequency ($\omega_{h,1}$) varies from 0.34 Hz using experimental data (i.e. pressure tests) to 0.36 Hz (+5%) and 0.27 Hz (-22%), using $\gamma - R_{\widetilde{\theta},t}$-SA and *SA-fully turbulent* approaches, respectively. Similarly, the first symmetrical torsional frequency ($\omega_{\alpha,1}$) varies from 0.56 Hz using experimental data, to 0.59 Hz (+4%) and 0.44 Hz (-21%), using $\gamma - R_{\widetilde{\theta},t}$-SA and *SA-fully turbulent* approaches, respectively.

The first asymmetrical vertical frequency ($\omega_{h,1}$) varies from 0.33 Hz using experimental data (i.e. pressure tests), to 0.35 Hz (+5%) and 0.26 Hz (-23%), using $\gamma - R_{\widetilde{\theta},t}$-SA and *SA-fully turbulent* approaches, respectively. Similarly, the first asymmetrical torsional frequency ($\omega_{\alpha,1}$) varies from 0.55 Hz using experimental data (i.e. pressures tests), to 0.58 Hz (-4%) and 0.43 Hz (+21%), using $\gamma - R_{\widetilde{\theta},t}$-SA and *SA-fully turbulent* approaches, respectively.

These results evidence that the $\gamma - R_{\widetilde{\theta},t}$-SA is a (reliable) affordable approach to evaluate the natural frequencies.

The symmetrical modal shapes estimated, using experimental values, are illustrated in Fig.15a and b, whereas panels (c) and (d) show the vertical displacements (δ) and rotations (α_x) of the deck regarding the longitudinal bridge axis for significant modes 0. The modal shape functions were normalized so that the norm of the discrete eigenvector is equal to one. The difference in terms of mass and natural frequencies given by $\gamma - R_{\widetilde{\theta},t}$-SA is between 5% and 10%, while it is between 21% and 47% using *SA-fully turbulent*, respectively. These structural quantities (i.e. mass and frequency) affect the flutter critical speed that in this paper is also used as measure of variability of the structural performance predictions by using the two investigated numerical approaches. Since the pressure distribution analyses and the load balance measurements were carried out as a static test, the flutter critical speed was estimated using quasi-static equivalent method [37] , [41] .

In particular, the critical flutter speed was estimated using two different approaches: firstly, nonlinear dynamic analysis by three-dimensional finite element models and quasi-static approximation of the unsteady wind loads (i.e. lift, drag and moment derived from the wind tunnel tests) were employed; secondly , a two-mode (2-DOF) generalized numerical model of the deck motion in the frequency domain and flutter derivatives were considered to better examine bridge aeroelasticity.

7.2 Deterministic flutter analysis.

7.2.1 FEM analysis

The first set of MDOF (i.e. Multi Degree of Freedom) analyses were carried out on a FEM model using experimental aerodynamic coefficients both directly estimated by the wind tunnel tests (Section 2.2) and evaluated from pressure coefficients (Section 2.1) [41]. Analyses were then repeated using aerodynamic coefficients resulting from the numerical CFD approaches (Fig. 9). As previously discussed, the critical flutter speed was estimated using a non-commercial nonlinear geometrical analysis software and by calculating dynamic analyses using step-by-step integration of the nonlinear three-dimensional structure with geometric nonlinearities. The global stiffness matrix was updated at each load step by assembling the stiffness sub-matrices of the elements, updated to account for the strain calculated at the previous time step.

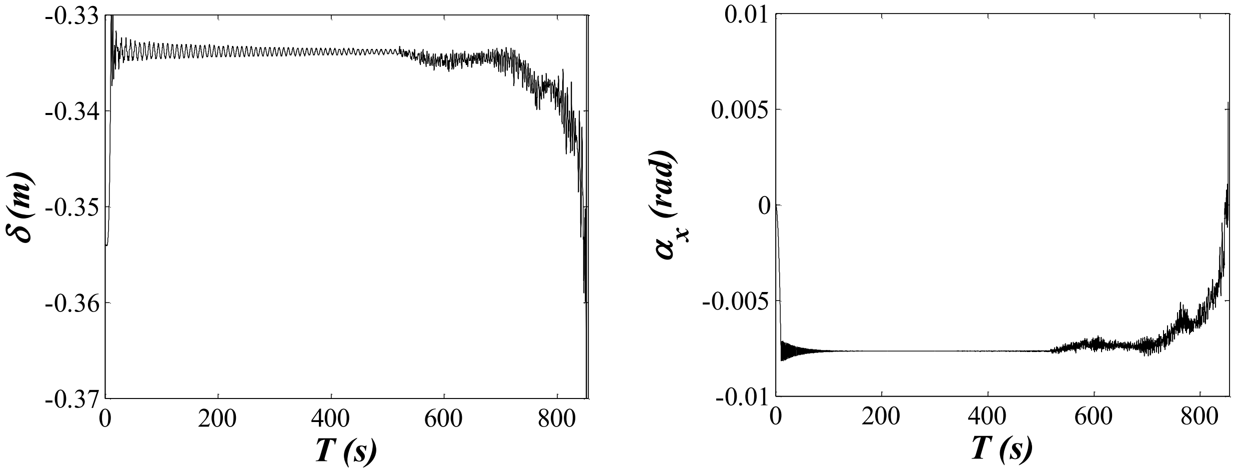

(a) Vertical displacements under critical flutter instability.

(b) Rotations of the deck about the longitudinal bridge axis under critical flutter instability.

Fig. 16 The time history of the deck vertical displacements and the rotation along the bridge longitudinal axis under the flutter instability is shown. This condition is estimated varying step by step the wind velocity and repeating non-linear analyses.

The under gravity loads solution was subsequently used as the initial step of the dynamic wind load analysis. The Newmark-Beta method with Rayleigh damping was used for numerical integration of the dynamic equations. Wind loads on the bridge deck were simulated by applying the aerodynamic coefficients (i.e. C_D, C_L and C_M) as a function of the time-dependent angle of attack and by setting the appropriate values of kinetic wind pressure at a given U. The program evaluated displacements and rotations of the bridge deck at progressively increasing values of U, and recorded the velocity at incipient flutter when reference deck rotations exceeded ±4° 0. As an example, Fig. 16 illustrates time histories of flutter instability in terms of vertical deck displacement (δ) and rotation (α_x), for the middle span section estimated using experimental values [40-46].

7.2.2Equivalent 2-DOF Scanlan's numerical model

It is worth noting that the main aeroelastic forces, that are induced by the motion of the deck and that affect the flutter instability, are the L_h lift force and the M_α overturning moment (Eqs. 26 and 27); they are usually expressed per unit deck length, measured on a model of span length l and based on the formulation by Scanlan and Tomko (1971) [16]. The H_i^* and A_i^* quantities (with i=1,…,4) are the flutter derivatives that depend on the reduced frequency $K=\omega B/U$ with ω being the angular vibration frequency of the deck and $n=\omega/(2\pi)$ the frequency in Hz.

$$L_h = \frac{1}{2}\rho U^2 B \left[KH_1\ (K)\frac{\dot{h}}{U} + KH_2\ (K)\frac{B\dot{\alpha}}{U} + K^2 H_3\ (K)\alpha + K^2 H_4\ (K)\frac{h}{B}\right], \tag{26}$$

$$M_\alpha = \frac{1}{2}\rho U^2 B^2 \left[KA_1\ (K)\frac{\dot{h}}{U} + KA_2\ (K)\frac{B\dot{\alpha}}{U} + K^2 A_3\ (K)\alpha + K^2 A_4\ (K)\frac{h}{B}\right]. \tag{27}$$

In Eqs. 26 and 27, ρ is the air density, U the mean wind speed perpendicular to the bridge model axis, B is the deck width; the over-dot symbol denotes derivation with respect to time t. Eqs. 26 and 27 must be modified to enable estimation of critical flutter speed in the frequency domain. Critical flutter is determined from a coincident condition with the simple harmonic motion of the deck, coupled with vertical and torsional motion (DOFs). This condition is determined by the total damping of a 2-DOF generalized model, which takes into account aeroelastic load contributions and simulates the two fundamental vertical and torsional modes of the deck. The procedure of the critical flutter speed calculation is recursive and the method is described in [16]. In the present paper, results were estimated using the quasi-static approximation of flutter derivatives, proposed by [37] . This allowed for an estimation of the $H_i \ \wedge A_i$, derivatives with $i = 1,2,3$ (Eqs.26 and 27) as a function of $K=2\pi nB/U$ and aerodynamic coefficients. Flutter calculations were conducted by neglecting the contribution of H_4 H_4 and A_4 . Solution to the flutter problem using the 2-DOF generalized model ([16]) can be obtained by transforming the differential system into a system of two complex-valued algebraic equations. After imposing the flutter condition, the roots of these two algebraic equations ([16]) can be found numerically.

The procedure provides a recursive method: at first setting the value of the K reduced frequency and then finding the root of each equation assuming Xvariable; the ω_c quantity is the critical angular flutter frequency and ω_h is the natural angular frequency of the vertical DOF or deck mode. The procedure is repeated until the same root X is found in both equations.

As was expected, there was a significant difference in critical flutter speed (U_c) values between MDOF and 2DOF calculations since there is a significant difference between results obtained applying experimental aerodynamic coefficients calculated by pressure coefficients (Figs.11 and 12) or aerodynamic forces (Fig.13). Table 4 lists the U_c values respectively for MDOF and 2DOF calculations using both the experimental datasets (i.e. pressure and aerodynamic forces) and the two CFD numerical data sets.

Table 4
Flutter critical speed U_c (m/s).

Data set	analyses	
	MDOF	2DOF
Aerodynamic forces wind tunnel experiments	129.0	164.2
Pressure wind tunnel experiments	107.4	138.3
$\gamma - R_{\widetilde{\theta},t}$-SA	105.2	134.5
SA – fully turbulent	114.7	152.2

As expected, results showed that the critical flutter speed estimated by CFD approaches is more in agreement with those estimated using experimental pressure tests than experimental load balance static tests. This is because the force loads derived from the CFD (Fig.14) were estimated integrating 2D pressure distributions around the deck in a similar way to pressure distributions from experimental tests. The fact that there is good agreement between experimental and numerical by $\gamma - R_{\widetilde{\theta},t}$-SA pressure coefficients trend is confirmed by flutter analyses results too. The $\gamma - R_{\widetilde{\theta},t}$-SA slightly underestimated the critical flutter speed using both MDOF FEM analyses (-2%) and 2DOF calculation (-3%) because it gave a slightly smaller mass. On the contrary, the significant difference of the deck mass given by *SA – fully turbulent* and its overestimation of pressure coefficients (Figs.12 and 13), affected the flutter analyses results. It gave greater values than experimental values for both, MDOF and 2DOF calculations, +7% and +10%, respectively. In the specific case study, the flutter critical speed was very high and this excluded the risk of flutter instability phenomena. However, the overestimation of critical condition reduces reliability.

7. Conclusion

This paper presents, for the first time, numerical computations based on Spalart-Allmaras local correlation based transition model (i.e. $\gamma - R_{\widetilde{\theta},t}$-SA) for Reynolds Averaged Navier-Stokes (RANS) equations for the flow past a bluff body. In particular, the numerical model was applied to a closed box section of a suspended bridge tested in two different wind tunnels. Experimental data were compared both with numerical results given by the proposed $\gamma - R_{\tilde{\theta},t}$-SA approach and also a Spalart-Allmaras fully turbulent model: results show a very good agreement for the $\gamma - R_{\tilde{\theta},t}$-SA model, although the fully turbulent model also seems to be able to capture the deck global behavior. In order to give a measure of error propagation due to the difference between numerical and experimental data on structural design, the critical flutter speed was evaluated using both pressure and aerodynamic coefficients given by numerical and experimental data. The critical flutter speed was estimated using both nonlinear analyses on a three-dimensional FEM model and numerical calculations of a 2DOF simplified model. Results showed that the $\gamma - R_{\tilde{\theta},t}$-SA model gives a critical flutter speed value closer to the experimental one with an error equal to about 8% less than SA-*fully turbulent*. In fact, the mean error percentage given by $\gamma - R_{\tilde{\theta},t}$-SA ranged between -3% to -2%, whereas the mean error in percentage given by SA-*fully turbulent* ranged between 7% to 10%. Results encourage researchers to extend comparisons with other case studies in order to confirm the accuracy of the $\gamma - R_{\tilde{\theta},t}$-SA.

Data Availability

Some or all data, models, or code that support the findings of this study are available from the corresponding author upon reasonable request.

References

[1] Bai Y., Sun D., LinJ..2010. Three dimensional numerical simulations of long-span bridge aerodynamics, using block-iterative coupling and DES. *Computers and Fluids* **39**, 1549–1561.

[2] Das S.N., Shiraishi S., Das S.K., 2010. Mathematical modeling of sway, roll and yaw motions: order-wise analysis to determine coupled characteristics and numerical simulation for restoring moment's sensitivity analysis. *Acta Mechanica*, **213**(3–4), 305–22.

[3] Parolini N., Quarteroni A., 2005. Mathematical models and numerical simulations for the America's cup. *Computer Methods in Applied Mechanics and Engineering*, **194**(9–11),1001–26.

[4] Ankush Rainaa G.A., Harmain Mir Irfan Ul Haqa, 2017. Numerical investigation of flow around a 3D bluff body using deflector plate.International *Journal of Mechanical Sciences*, 131–132,701-711.

[5] Jung S. Y., Kim J. J., Park H. W., Lee J. S., 2018. Comparison of flow structures behind rigid and flexible finite cylinders. *International Journal of Mechanical Science*, 142-143, 480-490.

[6] Martins F. A. C., Avilla J. P. J., 2019. Effects of the Reynolds number and structural damping on vortex-induced vibrations of elastically-mounted rigid cylinder. *International Journal of Mechanical Science*, 156, 235-249.

[7] Menter F. R., Langtry R.B., Volker S., 2006a. Transition modelling for general purpose CFD codes. *Flow, Turbulence and Combustion,* **77**, 277-303.

[8] Menter F.R., Langtry R., Likki S., Suzen Y., Huang P., Volker S., 2006b. A correlation based transition model using local variables – part 1: model formulation. *Journal of Turbomachinery* **128**, 413-422.

[9] Walters D. K., Cokljat D., 2008. A three-equation eddy-viscosity model Reynolds-Averaged Navier-Stokes simulations of transitional flow. *Journal Fluids Engineering, Transaction of the ASME*; **130** (12):1214011-12140114.

[10] Cid Montoya M., Nieto F., Álvarez A. J., Hernández S., Jurado J. Á.,Sánchez R.,2018. Numerical simulations of the aerodynamic response of circular segments with different corner angles by means of 2D URANS. Impact of turbulence modeling approaches. *Engineering Applications of Computational Fluid Mechanics*, **12**, 750–779.

[11] D'Alessandro V., GarbugliaF., MontelpareS., 2017a. A Spalart-Allmaras local correlation-based transition model for Thermo-fluid dynamics. *Journal of Physics*, Conference series **923** (2017) 012029.

[12] D'Alessandro V., Montelpare S., Ricci R., Zoppi A., 2017b. Numerical modeling of the flow past wind turbines airfoils by means of Spalart-Allmaras local correlation based transition model. *Energy*, **130**, 402-419.

[13] Spalart P.R., Jou W.H., Strelets M., Allmaras S.R., 1997. Comments on the feasibility of LES for wings, and on a hybrid RANS/LES approach. *Advances in DNS/ LES*. Greyden Press, 137–147.

[14] Spalart P.R., Squires K.D., 2004. The status of detached-Eddy simulation for bluff bodies. Direct and large Eddy simulation V. Springer. *The Aerodynamics of Heavy Vehicles: Trucks, Buses, and Trains*, Part of the Lecture Notes in Applied and Computational Mechanics book series (LNACM), **19**, 29-45

[15] Rizzo F., Caracoglia L., Montelpare S., 2018. Predicting the flutter speed of a pedestrian suspension bridge through examination of laboratory experimental errors. *Engineering Structures*, **172**, 589-613.

[16] Scanlan R.H., Tomko J.J., 1971. Airfoil and bridge deck flutter derivatives, *Journal of Engineering Mechanics, ASCE* 1971, **97**(EM6), 1717–37.

[17] Malan P., Suluksna K. and Juntasaro E., 2009. Calibrating the γ–Re_θ Transition Model for Comercial CFD. 47^{th} AIAA *Aerospace Sciences Meeting* (Orlando, FL).

[18] Patankar S. V., 1980. Numerical heat transfer and fluid flow. Series in computational methods in mechanics and thermal sciences, Washington: Hemisphere Pub. Corp., New York, ISBN 0-07-048740-5.

[19] Ferziger J.,Peric M., 1999. Computational Methods for Fluid Dynamics, ISBN 3-540-42074-6, Springer-Verlag Berlin Heidelberg, New York.

[20] Demirdzic I., Muzaferija S.,1995. Numerical method for coupled fluid flow, heat transfer and stress analysis using unstructured moving meshes with cells of arbitrary topology. *Computer Methods in Applied Mechanics and Engineering*, **125**, 235–55.

[21] Bruno L., Khris S., MarcillatJ., 2001. Contribution of numerical simulation to evaluating the effect of section details and partial streamlining on the aerodynamic behavior of bridge decks. *Wind and Structures*, Techno-Press, **4**, 315-332.

[22] Bruno L., Mancini G., 2002. The importance of Deck Details in Bridge Aerodynamics. *Structural Engineering International, Iabse*, **4**, 289-294.

[23] Fletcher, R. 1976. Watson, G. Alistair (ed.). "Conjugate gradient methods for indefinite systems". Numerical Analysis. Lecture Notes in Mathematics. Springer Berlin / Heidelberg. 506: 73–89. doi:10.1007/BFb0080109. ISBN . ISSN 1617-9692.

[24] Rizzo F.,Caracoglia L., 2018. Examining wind tunnel errors in Scanlan derivatives and flutter speed of a closed-box, *Journal of Wind and Structures*, **26**(4), 231-251.

[25] Blekherman A. N., 2005. Swaying of Pedestrian Bridges. *Journal of Bridge Engineering (ASCE)*, **10**(2), 1084-0702(2005)10:2(142).

[26] Scotta R., Lazzari R., Stecca E., Cotela, J., Rossi, R., 2006. Numerical wind tunnel for aerodynamic and aeroelastic characterization of bridge decks. *Computers and Structures*, **167**, 96-114.

[27] Ricciardelli F., Hangan H., 2001. Pressure distribution and aerodynamic forces on stationary box bridge sections. *Wind and Structures*, **4**, 399-412.

[28] Ricciardelli F., de Grenet E.T, Hangan H., 2002. Pressure distribution, aerodynamic forces and dynamic response of box bridge sections. *Journal of Wind Engineering and Industrial Aerodynamics*, **90**(10), 1135-1150.

[29] Augusti G., Spinelli P., Borri C., Bartoli G., Giachi M., Giordano S., 1995. The C.R.I.A.C.I.V. Atmospheric Boundary Layer Wind Tunnel. *Proceeding of the 9th International Conference on Wind Engineering*, New Delhi. Wiley Eastern Ltd.

[30] Belloli M., Fossati F., Giappino S., Muggiasca S., 2014. Vortex induced vibrations of a bridge deck: Dynamic response and surface pressure distribution. *Journal of Wind Engineering and Industrial Aerodynamics*, **133**,160-168.

[31] Suresh Kumar K., Stathopoulos T., 2000. Wind loads on low building roofs: A stochastic perspective. *Journal of Structural Engineering*, **126**, 944–956.

[32] Imai, K., Yun, C.B., Maruyama, O., Shinozuka, M., (1989). Fundamentals of system identification in structural dynamics. *Probabilistic Engineering Mechanics*, **4**(4), 162–173.

[33] Rizzo F., Ricciardelli F., Maddaloni G., Bonati A., Occhiuzzi A., 2020. Experimental error analysis of dynamic properties for a reduced-scale high-rise building model and implications on full-scale behavior. *Journal of Building Engineering*, 28.

[34] Zasso A., Stoyanoff S., Diana G., Vullo E., Khazem D., Pagani K.S.A., Argentini T., Rosa L., Dallaire, P.O., 2013. Validation analyses of integrated procedures for evaluation of stability, buffeting response and wind loads on the Messina bridge. *Journal of Wind Engineering and Industrial Aerodynamics*, **122**, 50–59.

[35] Xiang H. F., Ge Y.J., 2002. Refinements on aerodynamic stability analysis of super long-span bridges. *Journal of Wind Engineering and Industrial Aerodynamics*, **90**, 1493–1515.

[36] Cheng J., Cai C.S., Xiao R.C., Chen S.R., 2005. Flutter reliability analysis of suspension bridges. *Journal Wind Engineering and Industrial Aerodynamics* **93**, 757–775.

[37] Scanlan R. H., Jones N. P., Singh L., 1997. Inter-relations among flutter derivatives. *Journal of Wind Engineering and Industrial Aerodynamics*, **69-71**, 829-837.

[38] Jones N. P.,Scanlan R.H., 2001. Theory and full-bridge modeling of wind response of cable-supported bridges, *Journal of Bridge Engineering*, ASCE, **6**(6), 365-375.

[39] EN 1993-1-1 (2005). Eurocode 3: Design of steel structures - Part 1-1: General rules and rules for buildings. The European Union Per Regulation 305/2011.

[40] Kim, H.-K., Shinozuka, M., and Chang, S.-P. (2004). Geometrically nonlinear buffeting response of a cable-stayed bridge. *Journal of Engineering Mechanics*, ASCE, 130(7), 848-857.

[41] Singh L., 1997. Experimental determination of aeroelastic and aerodynamic parameters of long-span bridges. PhD Dissertation. Baltimore, Maryland, USA: Johns Hopkins University.

[42] Huang M. H., Thambiratnam D. P., Perera N. J., 2007. Dynamic performance of slender suspension footbridges under eccentric walking dynamic loads. *Journal of Sound and Vibration*, **303**(1- 2), 239-254.

[43] Lau C. K., Wong K. Y., 1997. Aerodynamic stability of Tsing Ma Bridge. Proceedings of the Fourth International Kerensky Conference on Structures in the New Millennium, Hong Kong, China.

[44] Pourzeynail S., Datta T. K., 2002. Reliability analysis of suspension bridges against flutter. *Journal of Sound Vibration*, **254**, 143–162.

[45] Franciosi C., Franciosi V., 1989. Second order influence line analysis of suspension bridges *International Journal of Mechanical Sciences,* **31**(8), 1989, 599-609.

[46] Bell A. J., Brotton D. M., 1973. A numerical integration method for the determination of flutter speeds. *International Journal of Mechanical Sciences*, **15**(6), 473-483.